

The survey of DA double white dwarf candidates based on DESI EDR

Ziyue Jiang (蒋子悦)^{1,2}, Hailong Yuan (袁海龙)¹, Zhongrui Bai (白仲瑞)¹, Mingkuan Yang (杨明宽)^{1,2}, Xiaozhen Yang (杨肖振)^{1,2}, Qian Liu (刘倩)^{1,2}, Yuji He (何玉吉)^{1,2}, Ganyu Li (李甘雨)^{1,2}, Yiqiao Dong (董义乔)¹, Mengxin Wang (汪梦欣)¹, Ming Zhou (周明)¹ and Haotong Zhang(张昊彤)¹

¹ Key Laboratory of Optical Astronomy, National Astronomical Observatories, Chinese Academy of Sciences, Beijing 100101, China

e-mail: htzhang@bao.ac.cn, yuanhl@bao.ac.cn

² School of Astronomy and Space Science, University of Chinese Academy of Sciences, Beijing 100049, China

Received 21 Jan, 2025; accepted 22 May, 2025

ABSTRACT

Aims. Mergers of double white dwarfs (DWDs) are considered significant potential progenitors of type Ia supernovae (SNe Ia), which serve as “standard candles” in cosmology to measure the expansion rate of the Universe and explore the nature of dark energy. Although there is no direct observational evidence to definitively determine the formation pathways of SNe Ia, studying the physical properties of DWDs provides valuable insights into their evolutionary processes, interaction modes, and merger mechanisms, which are essential for understanding the explosion mechanisms of SNe Ia. This study aims to identify DWD candidates through spectroscopic radial velocity (RV) measurements and analyze their physical properties based on DESI EDR.

Methods. We crossmatched DESI EDR with the *Gaia* EDR3 white dwarf (WD) catalog to select DA spectra. We measured the spectroscopic RV using the cross-correlation function (CCF) and assessed the significance of RV variability using a chi-squared-based variability method. Spectroscopic T_{eff} and $\log g$ were derived by fitting the hydrogen Balmer lines, with 3D convection corrections applied. Orbital periods and semi-amplitudes were obtained through a Lomb-Scargle analysis of the RV time series. We interpolated WD cooling models and applied Monte Carlo simulations to calculate masses, cooling ages, radii, and their associated uncertainties. Additionally, we analyzed their photometric and spectral energy distribution properties to derive photometric temperatures and radii, which were then compared with the corresponding spectroscopic parameters.

Results. We identified 33 DA DWD candidates with significant RV variability, including 28 new discoveries. Among them, we found an extremely low-mass DWD candidate and a potential triple system. For these candidates, we measured key physical parameters including T_{eff} , $\log g$, mass, and radius, and estimated the orbital periods based on the available data. Of these, 17 candidates exhibit relatively clear periodic RV variability in the current data, and we report their best-fitting periods and RV semi-amplitudes.

Key words. stars: white dwarfs – binaries: spectroscopic – techniques: radial velocities

1. Introduction

White dwarfs (WDs) represent the final evolutionary stage of stars, typically originating from stars with initial mass less than $8M_{\odot}$ (Althaus et al. 2010). After exhausting their nuclear fuel, the stars pass through the red giant phase, shed their outer layers with the remaining core gradually cooling and eventually evolve into WDs. Based on atmospheric composition and spectral features, WDs are primarily categorized into the hydrogen-dominated atmosphere white dwarf (DA), neutral helium (He I)-dominated atmosphere white dwarf (DB), continuous spectrum white dwarf (DC), ionized helium (He II)-dominated atmosphere white dwarf (DO), carbon-rich atmosphere white dwarf (DQ), metal-rich atmosphere white dwarf (DZ), and other less common types (Liebert & Sion 1994; McCook & Sion 1999; Kleinman et al. 2004; Gentile Fusillo et al. 2019). Among these, we focused on DAs, the most common WDs (Bergeron et al. 1992; Liebert et al. 2005; Torres et al. 2023), which are readily identifiable through observations and easier to model due to their high occurrence rate and well-defined hydrogen-rich spectral features.

Type Ia supernovae (SNe Ia) are renowned for their consistent luminosity and spectral features, and regarded as “standard candles,” enabling precise cosmic distance measurements. Their observations have revealed the accelerating expansion of the Universe, establishing dark energy as a cornerstone of cosmology and a key tool for studying cosmic structure and evolution (Riess et al. 1998; Perlmutter et al. 1999; Caldwell 2002; Riess et al. 2004; Planck Collaboration et al. 2016). It is widely accepted that SNe Ia result from thermonuclear explosions of WDs in binary systems when their masses reach the Chandrasekhar limit (Hoyle & Fowler 1960; Liu et al. 2023). Two primary progenitor scenarios are widely considered. One is the classic single-degenerate model, in which a WD accretes material from a non-degenerate companion until its mass reaches the Chandrasekhar limit, triggering thermonuclear explosions (Whelan & Iben 1973; Nomoto et al. 1984; Han & Podsiadlowski 2004). The other is the classic double-degenerate model, whereby two WDs in a binary system experience orbital shrinkage due to gravitational wave radiation, eventually merging and surpassing the Chandrasekhar limit to trigger thermonuclear explosions (Webbink 1984; Iben & Tutukov 1984; Badenes & Maoz 2012;

Maoz et al. 2014; Liu et al. 2018). Additional pathways, such as the super-Chandrasekhar mass model, sub-Chandrasekhar mass model, and other special progenitor scenarios such as the core-degenerate model and dynamically driven double-degenerate double-detonation (D^2) model, have also been proposed (Kashi & Soker 2011; Maoz & Mannucci 2012; Wang & Han 2012; Shen et al. 2018; Liu et al. 2023; Werner et al. 2024). However, there is still a lack of consensus on the specific properties of SNe Ia progenitors and their explosion mechanisms (Hillebrandt et al. 2013; Maeda & Terada 2016; Soker 2019; Liu et al. 2023). The type Iax supernova (SN Iax) is a distinct subclass of SNe Ia, distinguished by its lower luminosity and unique spectral characteristics (Foley et al. 2013). Potential progenitors include single-degenerate (such as a WD+He star, linked to LP 40-365), double-degenerate, and other models, partially explaining their properties (Wang et al. 2013; Vennes et al. 2017; Raddi et al. 2019). However, like SNe Ia, the specific progenitor systems and explosion mechanisms of SNe Iax still remain incompletely understood.

We are particularly interested in the double white dwarf (DWD) merger channel, which plays a crucial role in various areas of astronomical research. Yungelson et al. (1994) predicted that the merger rate of DWDs with a total mass exceeding the Chandrasekhar limit matches the formation rate of SNe Ia. Moreover, DWDs are not only potential progenitors of SNe Ia but also ideal gravitational wave sources for space-based observatories (Liebert et al. 2005; Li et al. 2020; Ren et al. 2023; Georgousi et al. 2023). Studying DWDs can also reveal the physical mechanisms governing the evolution from common envelope phases to binary mergers (Han et al. 1995; Livio & Soker 1988; Li et al. 2023). Currently, more than 300 DWDs have been identified, accounting for less than 5% of the over 30,000 known WDs (Munday et al. 2024). However, DWDs should account for about 10% of the total WD population in the Milky Way, according to the incomplete statistics from Maxted & Marsh (1999); Maoz & Hallakoun (2017); Napiwotzki et al. (2020); Korol et al. (2022); O'Brien et al. (2024); Munday et al. (2024). This significant discrepancy arises because WDs are faint and difficult to detect. Additionally, their broad spectral absorption lines require extensive high-resolution spectra to precisely measure and confirm radial velocities (RVs) and their variability. Therefore, it is challenging to find double-degenerate progenitors, especially for low-resolution spectra (Rebassa-Mansergas et al. 2019), which also indicates that numerous undiscovered DWDs await further investigation and exploration.

Spectral fitting of RV and atmospheric parameters is one of the most common methods of studying DWDs. As early as two to three decades ago, Saffer et al. (1988), Foss (1989), Bragaglia et al. (1990), Marsh (1995), and Maxted et al. (2000) searched for DWDs and their candidates by identifying RV variability, although the sample size was limited at that time. The advent of large-scale new-generation spectroscopic surveys has yielded a wealth of high-quality WD spectra. To test the double-degenerate channel for SNe Ia formation, the ESO Supernova Ia Progenitor Survey (SPY) (Koester et al. 2001; Napiwotzki et al. 2001) initiated large-scale RV measurements of WDs from the early 21st century, leading to the discovery of over 80 DWDs to date (Nelemans et al. 2005; Koester et al. 2009; Napiwotzki et al. 2020). Extremely low-mass (ELM) WDs, with masses of less than $0.3M_{\odot}$ (Pylyser & Savonije 1988; Li et al. 2019; Yuan et al. 2023b), are considered key candidates for DWDs. Brown et al. (2010) launched the ELM Survey in the Sloan Digital Sky Survey (SDSS). Together with the ELM Survey South by Kosakowski et al. (2020), these efforts have identified about

150 DWDs (Brown et al. 2020, 2022; Kosakowski et al. 2023). Yan et al. (2024) also used RV variability and identified 56 newly discovered DWD candidates based on SDSS DR14 spectra. Additionally, Munday et al. (2024) initiated the double-lined DWD (DBL) survey, targeting relatively over-luminous sources in the WD cooling sequence based on *Gaia* colors, and identified 34 double-lined systems through spectral fitting. Munday et al. (2024) also created the CloseDWDbinaries database, which contains over 300 identified DWDs, including 77 double-lined systems. Other large-scale projects, such as the Large Sky Area Multi-Object Fiber Spectroscopy Telescope (LAMOST), also include studies on DWDs (Yuan et al. 2023a).

Most DWDs exhibit weak photometric variability, making them difficult to detect by photometric surveys such as the Zwicky Transient Facility (ZTF) and the one conducted by the Transiting Exoplanet Survey Satellite (TESS) (Sousa et al. 2024). But photometric searches have still led to some significant discoveries, particularly in detecting short-period variable sources. Steinfadt et al. (2010) reported the discovery of the first eclipsing detached DWD NLTT 11748 through pulsation searches. Bours et al. (2014) discovered the first double-lined eclipsing DWD CSS 41177 and provided the masses and radii of the binary system, through combined modeling of the light curves from ULTRACAM and the RV from X-Shooter. ZTF has also identified more than ten DWDs to date (Burdge et al. 2020; Keller et al. 2022; Ren et al. 2023), including ZTF J153932.16+502738.8 with an orbital period of 6.9 min and ZTF J2243+5242 with an orbital period of 8.8 min (Burdge et al. 2019, 2020). Munday et al. (2023) also discovered the third-closest eclipsing DWD WDJ022558.21-692025.38 with a distance of approximately 400 pc and an orbital period of 47.19 min, based on TESS. Korol et al. (2017) predicted that the powerful photometric capabilities of *Gaia* and the Large Synoptic Survey Telescope (LSST) will detect hundreds to thousands of short-period eclipsing DWDs.

In addition to the two commonly used methods mentioned above, there are other approaches for searching for DWDs. El-Badry et al. (2021) utilized the high-precision parallax (plx) and proper motion (pm) data from *Gaia* EDR3 to obtain a sample of over 1 million binary systems, which included 1565 DWD candidates. Similarly, Torres et al. (2022) identified wide-separation WD binary systems within 100 pc, also based on *Gaia* EDR3, comprising 155 DWD candidates, and conducted an in-depth study by population synthesis fitting. Moreover, with the future deployment of gravitational wave detectors such as the Laser Interferometer Space Antenna (LISA), more DWDs might be detected through their gravitational wave radiation, and the dual detection of electromagnetic waves and gravitational waves will also become feasible (Korol et al. 2017; Breivik et al. 2018; Jin et al. 2025).

In this study, we searched for DWD candidates from the Dark Energy Spectroscopic Instrument Early Data Release (DESI EDR) (Adame et al. 2024), using RV variability. The structure of this paper is as follows. Section 2 introduces the data sources and the criteria and methods for sample selection. Section 3 details the methods and results of measuring RV and its variability, as well as of determining T_{eff} and $\log g$. Section 4 describes the calculation process for orbital parameters such as period and semi-amplitude. Section 5 explores the light curves and performed spectral energy distribution (SED) fitting. Section 6 further discusses the results presented earlier, including an ELM DWD candidate, five known sources, and a potential triple-star system. Finally, Section 7 summarizes the paper.

2. Data

DESI is one of the largest spectroscopic survey projects currently being undertaken (Dey et al. 2019). While its primary mission is to explore dark energy and the structure of the Universe, the highly efficient spectroscopic data acquisition capabilities of DESI have also provided a wealth of resources for stellar research. DESI's spectra cover a wavelength range from 3600 Å to 9800 Å with a resolution range of 2000 to 5500.

In this study, we used the DESI EDR spectroscopic dataset, which covers survey validation observation data from December 2020 to June 2021, containing spectra recording of 1.8 million unique targets, including 496,128 star sources (Adame et al. 2024). To obtain WD spectra from DESI EDR STAR spectra, we referred to the WD candidate catalog provided by Gentile Fusillo et al. (2021), based on *Gaia* EDR3. This catalog used multiple selection criteria, including absolute magnitude, color index, *Gaia* quality flags, visual inspection, and probabilities of being a WD (P_{WD} (Gentile Fusillo et al. 2019)), ultimately identifying 1,280,266 reliable WD candidates.

By cross-matching DESI EDR STAR spectra with the *Gaia* EDR3 WD candidates catalog, we obtained 812 WD targets and 7631 corresponding single-exposure spectra. Due to low signal-to-noise ratios (S/Ns), which introduce significant errors in RV measurements, we computed the median S/N for each spectrum and set a threshold of 10 to filter the data. This improved the accuracy of RV calculations, while retaining as many candidate spectra as possible.

As a result, we selected 332 DAs with 2839 spectra. The exposure time ranges from 60 s to 1800 s, with most falling between 250 s and 1400 s. The observation time span for each source ranges from half an hour to 140 days. The positions of these 332 sources and 33 DWD candidates (see Section 3.4) on the Hertzsprung-Russell (HR) diagram are shown in Figure 1.

3. Spectral measurements

3.1. Effective temperature and surface gravity

We used the Python tool *wdtools* (Chandra et al. 2020; Chandra 2020) to fit the spectra of DAs in order to determine T_{eff} , $\log g$, and their associated errors. The package fits the hydrogen Balmer lines (in this study, $H\alpha$, $H\beta$, $H\gamma$, $H\delta$, and $H\epsilon$) and interpolates the templates provided by Koester (2010) using a high-speed neural network. It combines the Markov chain Monte Carlo (MCMC) sampling method to derive the atmospheric parameters of WDs, effectively improving the precision of the parameter estimation. Figure 2 illustrates an example of *wdtools* results. Notably, *wdtools* shows relatively small uncertainties in T_{eff} and $\log g$ for single-exposure spectra, solely reflecting measurement errors from MCMC simulations, without implying any physical significance. When calculating the final error for an individual source, we combined the single-spectrum measurement errors and the standard deviation across multiple observations. The final error was calculated from Equation 1:

$$\text{error} = \sqrt{\bar{\epsilon}^2 + \text{std}^2}, \quad (1)$$

where $\bar{\epsilon}$ represents the mean of single-exposure spectrum measurement errors, and std denotes the standard deviation across multiple spectra.

Tremblay et al. (2013) showed that 3D convective effects become particularly significant at lower temperatures (typically $T_{\text{eff}} < 15,000\text{K}$), leading to a systematic overestimation of $\log g$

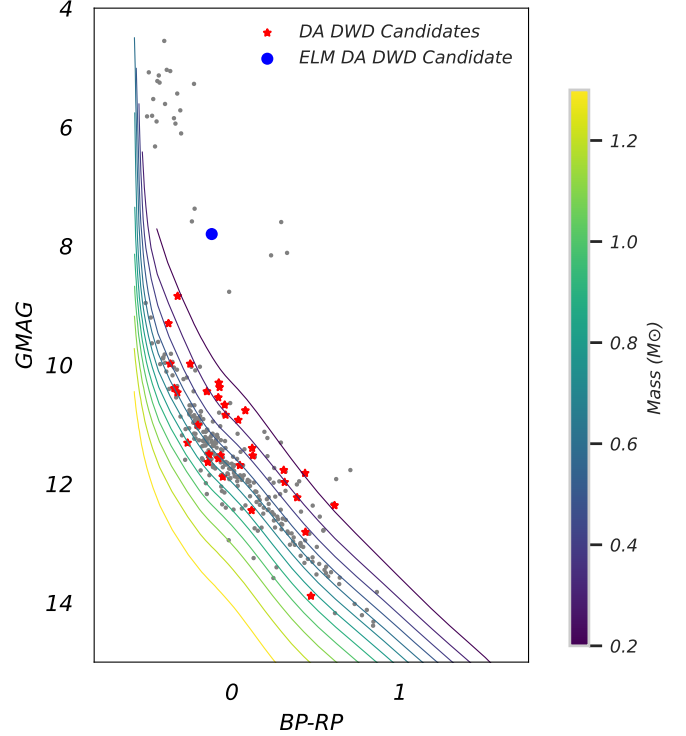


Fig. 1. HR diagram of 332 selected DA with $S/N > 10$. The red stars represent 32 DA DWD candidates, while the blue point represents the only ELM DA DWD candidate. All of these 33 sources exhibit significant RV variability. The cooling tracks were derived from the DA synthetic colors tables at astro.umontreal.ca/bergeron/CoolingModels/. Additionally, the cooling tracks are for single stars, while our candidates are binaries with a higher overall luminosity. Consequently, they fall in the region of the cooling tracks corresponding to lower masses than the ones in Section 4.1.

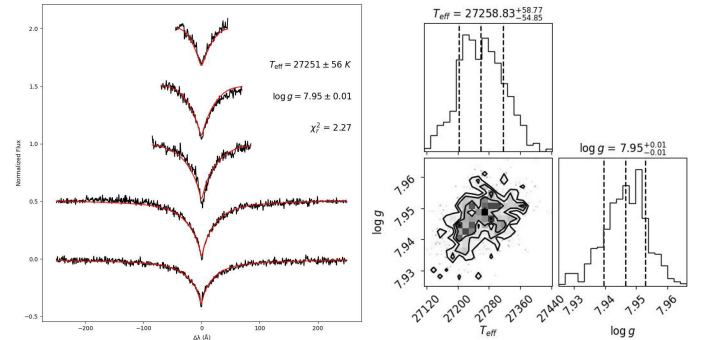


Fig. 2. Fitting and corner plot from *wdtools*. The left panel shows the fitting result of the hydrogen Balmer lines ($H\alpha$, $H\beta$, $H\gamma$, $H\delta$, and $H\epsilon$, from bottom to top) for the single-exposure spectrum of **WDJ084253.03+230025.47** at MJD = 59230.347393, yielding T_{eff} and $\log g$. The right panel is the corresponding corner plot, which illustrates the correlations between parameters and their marginal distributions, providing a visual representation of parameter uncertainties.

for cool WDs when inferred from the 1D models of Koester (2010). Consequently, we implemented corrections to the spectroscopic parameters of sources in the final results with $T_{\text{eff}} < 15,000\text{K}$, along with the corresponding errors derived from the standard deviation of 1000 simulations. Therefore, unless oth-

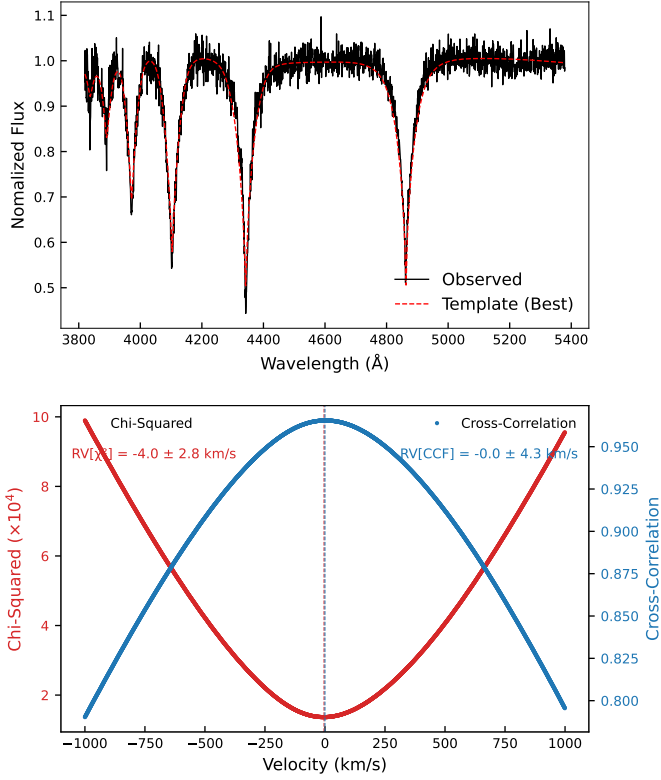


Fig. 3. Example of template matching and RV calculation using a single-exposure spectrum of **WDJ084253.03+230025.47** at MJD = 59230.357356. The top panel shows the matching of the normalized spectrum with the best template ($T_{\text{eff}} = 27,000$ and $\log g = 8.0$). The bottom panel displays the χ^2 curve and CCF curve obtained by shifting the best template. It can be seen that the RV results from the CCF and χ^2 curves are very close.

erwise specified, all spectroscopic parameters in the subsequent content have been corrected.

3.2. RV measurement

We measured the RV using a template-matching method with the WD spectral templates from [Koester \(2010\)](#), as was done in [Anguiano et al. \(2017\)](#). We first normalized the single-exposure spectra using a polynomial fitting method. Next, we matched the normalized single-exposure spectra in the wavelength range of 3800–5500 Å with the WD templates convolved and resampled to match the observational spectral resolution. The matching degree was evaluated using a chi-squared (χ^2) function, which allowed us to determine the optimal template. Subsequently, the optimal template was shifted within a velocity range of [-1000, 1000] km/s. The most likely RV was derived from χ^2 minimum and cross-correlation function (CCF) maximum ([Tonry & Davis 1979](#)). Figure 3 illustrates an example of template matching and RV calculation. The smooth χ^2 and CCF curves demonstrate the quality of the fitting and matching. The final RV was taken from the velocity at CCF maximum and the velocity at χ^2 minimum served as a secondary validation.

To ensure that spectral signal errors are accurately reflected in the RV errors, we adopted the error variance formula of CCF based on a maximum likelihood approach proposed by [Zucker](#)

(2003):

$$\sigma_s^2 = - \left[N \frac{C''(\hat{s})}{C(\hat{s})} \frac{C^2(\hat{s})}{1 - C^2(\hat{s})} \right]^{-1}, \quad (2)$$

where N is the number of RV measurements, $C(\hat{s})$ is the value of the CCF, and $C''(\hat{s})$ is the second derivative of the CCF. Specifically, the term $\frac{C''(\hat{s})}{C(\hat{s})}$ represents the sharpness of the CCF curve peak. A larger absolute value indicates a sharper peak and a smaller error. The term $\frac{C^2(\hat{s})}{1 - C^2(\hat{s})}$ is closely related to the S/N and reflects the impact of the sample error on the velocity error.

It is noteworthy that, due to the effects of pressure broadening and pressure shifts caused by the Stark effect, the RV measurement method proposed here is primarily suitable for subsequent variability measurements. Therefore, achieving precise RV measurements requires confirmation through high-resolution spectroscopy ([Napiwotzki et al. 2020](#); [Arseneau et al. 2024](#); [Raddi et al. 2025](#)).

3.3. Variability measurement

After measuring the RV of a WD from single-exposure spectra at different time, we applied the variability detection method based on χ^2 statistics proposed by [Maxted et al. \(2000\)](#) to further identify WDs with significant velocity variability. This method has been widely validated for its reliability and accuracy, particularly for analyzing velocity variability in binary systems.

For the v_i , the RV of the i -th single-exposure spectrum, we used the inverse square of its corresponding error $\frac{1}{\sigma_i^2}$, as the weight to calculate the weighted average velocity, \bar{v} :

$$\bar{v} = \frac{\sum_i \frac{v_i}{\sigma_i^2}}{\sum_i \frac{1}{\sigma_i^2}}. \quad (3.1)$$

Next, to quantify the deviation between v_i and the weighted average velocity, \bar{v} , we calculated χ_m^2 :

$$\chi_m^2 = \sum_i \left(\frac{v_i - \bar{v}}{\sigma_i} \right)^2. \quad (3.2)$$

We then calculated the P value corresponding to the χ^2 distribution with $n - 1$ degrees of freedom:

$$P(\chi^2 > \chi_m^2) = 1 - F(\chi_m^2, n - 1). \quad (3.3)$$

Here, n is the number of observations and $F(\chi_m^2, n - 1)$ represents the cumulative distribution function (CDF) of the χ^2 distribution. Finally, we calculated the variability index, η :

$$\eta = -\log_{10}(P). \quad (3.4)$$

From the above equations, it can be seen that a larger η leads to a smaller P , which in turn results in a larger χ_m^2 , indicating a more significant velocity variability. The specific workflow and results were detailed in Section 3.4.

3.4. Results

Considering the influence of the interval between WD template parameters, we adopted a multistep strategy involving preliminary and refined screening to minimize errors and accurately determine the RVs and their variability.

We first performed template matching on 2839 single-exposure spectra of 332 DAs, calculating the preliminary RV and

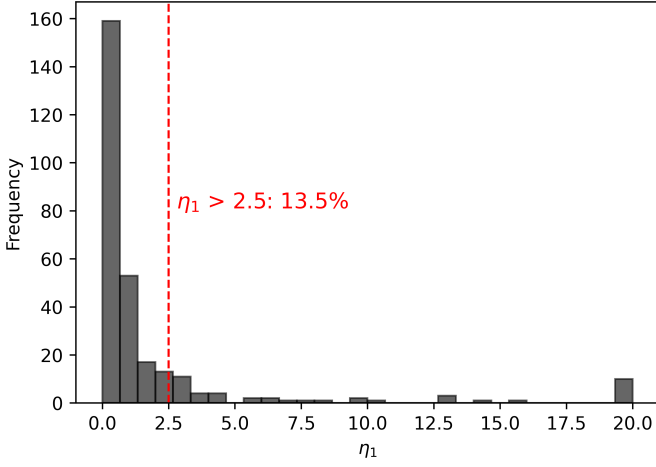


Fig. 4. Distribution histogram of η_1 values calculated from the RV of template matching. For convenience of plotting, values greater than 20 are capped at 20. In this distribution, about 13.5% of the sources have $\eta_1 > 2.5$. Considering the theoretical prediction of DWDs accounting for around 10% in the Milky Way (Maxted & Marsh 1999; Maoz & Hallakoun 2017; Napiwotzki et al. 2020; Korol et al. 2022; O’Brien et al. 2024; Munday et al. 2024) and the need for further selection, $\eta_1 > 2.5$ is a loose but reliable criterion.

η_1 (Equation 3.4). Figure 4 shows the distribution histogram of η_1 . Then, using the parameters from *Gaia* EDR3 (Gentile Fusillo et al. 2021), the median values and the mean values of T_{eff} and $\log g$ derived from the single-exposure spectra of each source with *wdtools*, respectively, we fixed three templates for each source. We calculated a set of RV and η for each template. Subsequently, we obtained three sets of RV and the corresponding η_2, η_3 , and η_4 . Finally, we adopted $\eta > 2.5$ (Equation 3.4) as the criterion for significant differences in the RV variability, taking the union of the four sets: $\eta_i > 2.5$ ($i = 1, 2, 3, 4$).

After the above steps, we initially selected 63 candidate sources. For each spectrum of the 63 sources, we visually inspected the corresponding templates and the Balmer lines fit by *wdtools*, excluding the spectra with poor fits. Then, we computed the weighted average of T_{eff} and $\log g$ obtained from each single-exposure spectrum, using the S/N as the weight, to determine the atmospheric parameters for each source. Finally, we fixed the templates using the latest obtained parameters, and recalculated the RV and the η_{final} values.

Subsequently, we selected 33 sources with $\eta_{\text{final}} > 2.5$ as the final list of DWD candidates, as is shown in Table A.1; their RV data are shown in Figure A.1. Additionally, we applied a velocity correction and performed inverse-variance weighted averaging on each single-exposure spectrum to obtain the coadded spectra. We used *wdtools* to fit the coadded spectra and compared the results with the weighted results from the single-exposure spectra. Figure 5 shows that the parameters remain consistent between the single-exposure spectra and the coadded spectra, as is shown in Figure A.2.

4. Masses and orbital parameters

4.1. Masses of candidates

To calculate the masses of WDs, we used *WD_models* (Cheng 2021) and *Montreal White Dwarf Database* (Dufour et al. 2017). These tools both rely on synthetic color and evolutionary

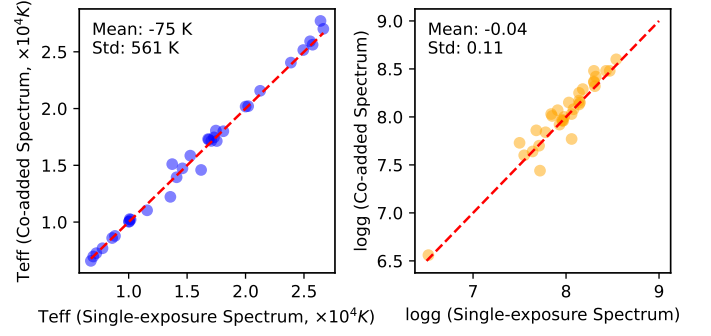


Fig. 5. Comparison plots between single-exposure spectra and coadded spectra. The parameters of single-exposure spectra are the weighted average of T_{eff} and $\log g$ obtained from each single-exposure spectrum, using the S/N as the weight. The parameters of coadded spectra are from *wdtools* fitting. The left panel shows T_{eff} , while the right panel displays $\log g$. And T_{eff} shows a mean difference of -75 K with a standard deviation of 561 K, while $\log g$ has a mean difference of -0.04 and a standard deviation of 0.11.

sequence tables of WDs, using interpolation methods to map the input values of T_{eff} and $\log g$ to parameters such as mass, cooling age, radius, and others. The former is an open-source Python package, while the latter is a convenient web application.

Different models were applied depending on the mass range of WDs when using *WD_models*. For low-mass models (less than about $0.5 M_{\odot}$) and middle-mass models (about 0.5 to $1.0 M_{\odot}$), we used the thick-H or He-atmosphere CO WD models from Bédard et al. (2020) available at astro.umontreal.ca/bergeron/CoolingModels/ (Kowalski & Saumon 2006; Holberg & Bergeron 2006; Tremblay et al. 2011; Blouin et al. 2017). For high-mass models (greater than $1.0 M_{\odot}$), we used the model for O/Ne-core WDs from Camisassa et al. (2019). For ELMs with $\log g < 7$, we used the He-core WD model provided by Althaus et al. (2013).

To estimate the errors of mass, cooling age, and radius, we employed the Monte Carlo sampling method. For each WD source, we assumed that the atmospheric parameters follow a normal distribution with the fit values of T_{eff} and $\log g$ as the mean and their corresponding error as the standard deviation. A Monte Carlo simulation was performed by generating 1000 random samples. Subsequently, we obtained the mass, cooling age, radius, and their respective uncertainties for 33 DA DWD candidates. Figure 6 shows the mass distribution of all candidates. There is one ELM, and no source with a mass greater than $1 M_{\odot}$. Table A.1 shows a portion of the results, with more detailed data presented in Data availability.

4.2. Periods

In our study, we applied the Lomb-Scargle (Lomb 1976; Scargle 1982) method to calculate the most likely periods of candidate systems. Since high-frequency (short-period) DWDs are more easily detectable and are more likely to serve as progenitors of SNe Ia (Breedt et al. 2017), we focused on searching for such systems. However, when setting the frequency parameters in Lomb-Scargle method, uniform sampling in frequency results in sparse coverage of long periods, hindering the detection of long-period DWDs. Conversely, uniform sampling in periods reduces sensitivity to short-period systems. To address this issue, we developed a segmented uniform sampling strategy in peri-

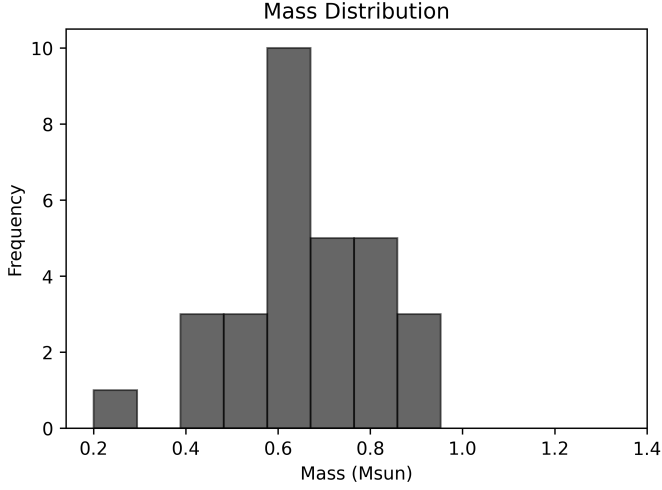


Fig. 6. Mass distribution histogram of DA DWD candidates. The masses of the candidates range from about $0.2M_{\odot}$ to $1M_{\odot}$, which is likely attributed to different evolutionary formation pathways. The peak is about $0.6M_{\odot}$, which is the typical DA mass (Tremblay et al. 2011; Kleinman et al. 2013; Kepler et al. 2015).

ods to balance the detection efficiency between short and long periods.

We evenly distributed sampling points across three period intervals: the step size is 10^{-7} days for $0.02 < p(\text{day}) < 1$ (as the maximum spectral exposure time is 1800 s, approximately 0.02 days, making periods shorter than 0.02 days probably unreliable), 10^{-6} days for $1 < p(\text{day}) < 10$, and 10^{-5} days for $10 < p(\text{day}) < 100$. Approximately 10^7 period points are generated in each interval and then converted to frequency points for Lomb-Scargle analysis. This distribution strategy ensures detailed coverage in the short-period range, while maintaining effective detection in the long-period range.

Due to the limited exposure times, which restricted the precision of Lomb-Scargle, we selected the five highest power points from the power spectrum as candidate periods for each source. To avoid power values becoming overly concentrated due to high-density sampling, we made the following adjustments to period selection. First, we ranked the frequencies in descending order of power and converted them to the corresponding periods. Next, to balance the distribution of high frequencies (short periods) and low frequencies (long periods), we adjusted the precision of the periods. Periods of less than 1 day were rounded to two decimal places (since periods shorter than 0.02 days are unreliable here, the minimum precision was set to 0.01 days), and periods of between 1 day and 100 days were rounded to one decimal place. Then, we removed duplicate periods, retaining only the unique period with the highest power, and recorded the period values with six decimal places of precision in the final list. Finally, we selected the five most significant periods from the power spectrum for each candidate, ensuring that they reflected the periodic features of the system. For the five candidate periods of each source, we further performed the trigonometric function fit and calculated the coefficient of determination (R^2).

Ultimately, we obtained five periods and their corresponding semi-amplitudes for each candidate. We assessed the reliability of each period by visually inspecting the fitting curves and R^2 , discarding periods with $R^2 < 0.8$. As a result, we obtained 17 DWD candidates with 1–5 well-fit periods. Detailed data and plots are presented in Table A.2 and Data availability. Addition-

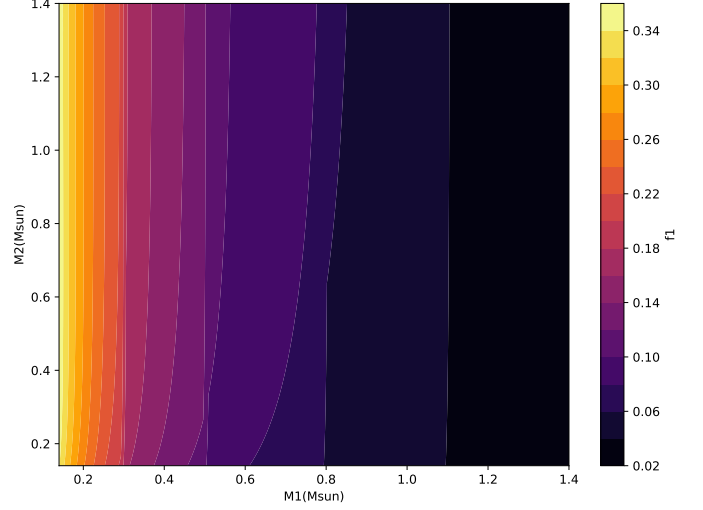


Fig. 7. Diagram showing how the Roche lobe filling degree of the primary star in a DWD system with a 30-minute orbital period varies with the binary mass. Here, $f_1 = \frac{R_1}{R_{L1}}$, where R_{L1} is the Roche lobe radius from Eggleton (1983).

ally, further RVs are required to confirm these values in a robust way, due to the limited current data.

5. Photometry

5.1. The search for light curves

We crossmatched 33 DA DWD candidates with the Zwicky Transient Facility (ZTF)(Bellm et al. 2019; Masci et al. 2019; Graham et al. 2019; Ofek et al. 2020), the All Sky Automated Survey for Supernovae (ASAS-SN)(Kochanek et al. 2017), the Transit Exoplanet Survey Satellite (TESS)(Ricker et al. 2015), the Catalina Real-Time Transient Survey(CRTS)(Drake et al. 2009), and the Wide Field Survey Telescope (WFST, “Mozi”)(Wang et al. 2023). However, we did not obtain any significant light curves through Lomb-Scargle period analysis and trigonometric fitting.

This is primarily because the eclipse probability of our candidates is low, and the ellipsoidal variation amplitude is small. First, most confirmed eclipsing DWD systems are compact binaries with extremely short periods. For instance, ZTF’s search for DWDs primarily focuses on systems with periods shorter than one hour(Keller et al. 2022), including the previously mentioned ZTF J153932.16+502738.8 with a period of 6.9 min and ZTF J224342.97+524205.9 with a period of 8.8 min (Burdge et al. 2019, 2020). Our detection has a minimum response period of approximately half an hour, so we were unable to detect candidates with periods shorter than this. Additionally, Figure 7 presented a simple simulation that we performed, revealing that in a DWD system with a 30-minute orbital period, the Roche lobe filling factor of the primary star is less than 0.36. According to Gommel et al. (2021), the ellipsoidal variation amplitude is smaller than 2% when the filling factor is less than 0.4, which is lower than most of the errors in the above photometric surveys. Therefore, in DWD systems with periods longer than half an hour, the ellipsoidal variation amplitude should be very small.

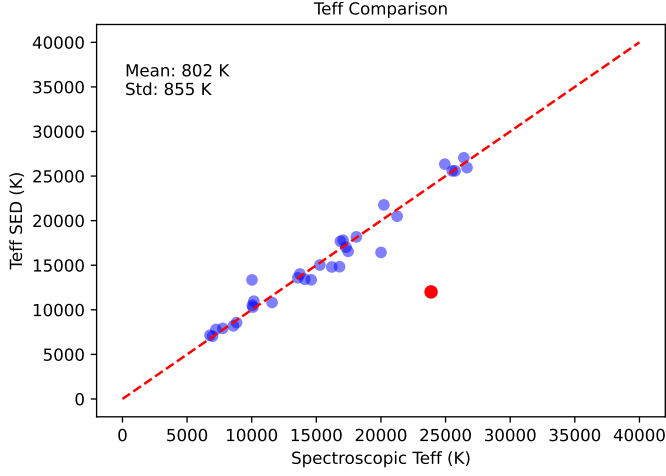


Fig. 8. Comparison plot between T_{eff} derived from the single-DA SED fitting and those obtained from previous spectral fitting. The red point in the plot represents the outlier **WDJ100236.84+023835.03** with significantly inconsistent temperatures, as is discussed in Section 6.1. Ignoring this outlier, the spectroscopic temperatures differ from the photometric temperatures by a mean difference of 802 K, with a standard deviation of 855 K.

5.2. SEDs

To further verify the accuracy of spectral fitting, we conducted the single-DA SED fitting for 32 selected DA DWD candidates. Notably, one of the 33 candidates lacked sufficient and reliable photometric data in **CDS**, as is discussed in Section 6.4. Consequently, we did not perform SED fitting for this source. We utilized a range of observational data across multiple wavelengths, including GALEX GR6+7 (filters: FUV, NUV) (Bianchi et al. 2017), SDSS DR16 (filter: u) (Ahumada et al. 2020), Pan-STARRS1 DR1 (filters: g, r, i, z, y) (Chambers et al. 2016), and Gaia DR3 (filters: BP, G, RP) (Gaia Collaboration et al. 2016, 2023). In addition, for the near-infrared coverage, we adopted data from one of the following surveys depending on availability: the 2MASS All-Sky Point Source Catalog (filters: J, H, Ks) (Cutri et al. 2003), UKIDSS-DR9 (filters: Y, J, H, K) (Lawrence et al. 2007), or UltraVISTA DR4 (filters: Y, J, H, Ks) (McCracken et al. 2012). The fitting was performed using the DA model spectra (Koester 2010). All SED fitting plots were presented in **Data availability**.

To eliminate the effects of interstellar extinction, we utilized the Python package *dustmaps* (Green 2018), which was used to obtain the $E(B - V)$ values from the 3D Bayestar model (Green et al. 2019). Bayestar was constructed using the photometric data from Pan-STARRS 1 for 800 million stars and partial stellar photometry data from 2MASS, covering a quarter of the sample (Green 2018). The plx values were from the Gaia WD catalog (Gentile Fusillo et al. 2021). As a result, we obtained the photometric temperatures and photometric radii of these candidates. And we compared the photometric temperatures with the spectroscopic temperatures, as is shown in Figure 8. Except for the outlier, these two temperatures are generally consistent.

Additionally, we calculated the spectroscopic radii by interpolating atmospheric parameters into the Montreal WD Database (Dufour et al. 2017) and compared them with the photometric radii, as is shown in panel c of Figure 9. Panel c indicates that the photometric radii we measured are significantly larger than the spectroscopic radii. To check our results, we ob-

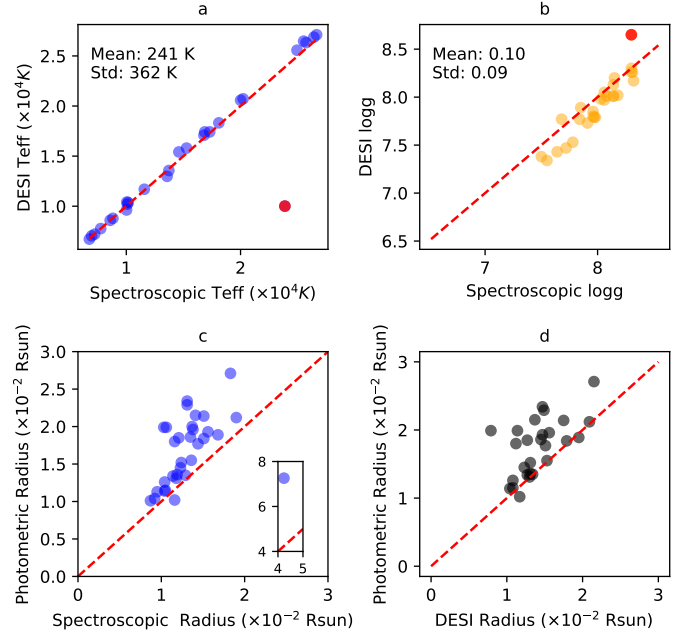


Fig. 9. a and b : Comparison plots between our spectroscopic parameters and those from Manser et al. (2024). The red point represents the outlier in Figure 8. Temporarily ignoring this outlier, our calculated T_{eff} and $\log g$ differ from their results by a mean difference of 241 K and 0.1, with a standard deviation of 362 K and 0.09, respectively, indicating a certain degree of consistency. Notably, six sources are not included in their catalog. c and d: Comparison plots of the spectroscopic radii calculated from our spectroscopic parameters and those from Manser et al. (2024), against the photometric radii. It is evident that the majority of photometric radii are larger than both sets of the spectroscopic radii.

tained the spectroscopic parameters from Manser et al. (2024), who also conducted a study of WDs based on DESI EDR spectra. Panel a and panel b of Figure 9 indicate that T_{eff} and $\log g$ from both catalogs are very close, except for the outlier. Since the value of the spectroscopic radius is highly sensitive to $\log g$, we recalculated the spectroscopic radii using their parameters and compared them with the photometric radii. Panel d confirms that the larger photometric radii were not caused by small deviations in $\log g$. These results further strengthen the case for our DWD candidates, as unresolved binary systems are often interpreted as single objects in SED fitting, leading to systematically overestimated photometric radii.

Considering the potential influence of a companion star, we conducted SED fitting using double-DA templates for these candidates. However, due to significant uncertainties in the results, we have opted not to present these findings here.

6. Discussion

In this section, we discuss some special candidates in detail, including a problematic candidate, an ELM, some crossmatched ELM candidates, some known candidates, and a potential triple-star system.

6.1. A problematic candidate

For the outlier **WDJ100236.84+023835.03** shown in Figure 8, we obtained its temperature of about 23,900 K, $\log g$ of 8.3, and radius of about $0.01R_{\odot}$ from both single-exposure and coadded

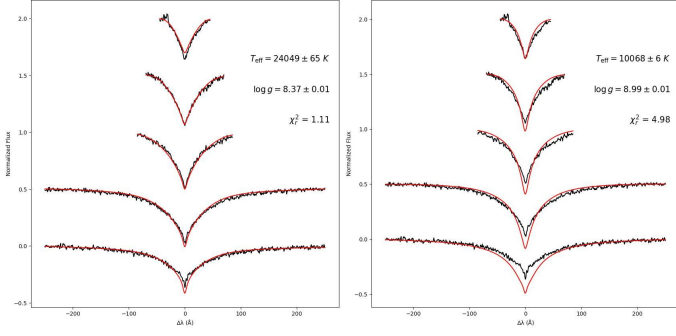


Fig. 10. Left panel: Best-fit result of the coadded spectrum of WDJ100236.84+023835.03 from *wdtools* without a temperature limit. Right panel: Best-fit result of the coadded spectrum of WDJ100236.84+023835.03 from *wdtools* with a temperature upper limit of 15,000 K. The results shown in the figure have not been corrected for 3D convective effects. After 3D correction, the results are 9992 K and 8.73, which is close to the results of Manser et al. (2024).

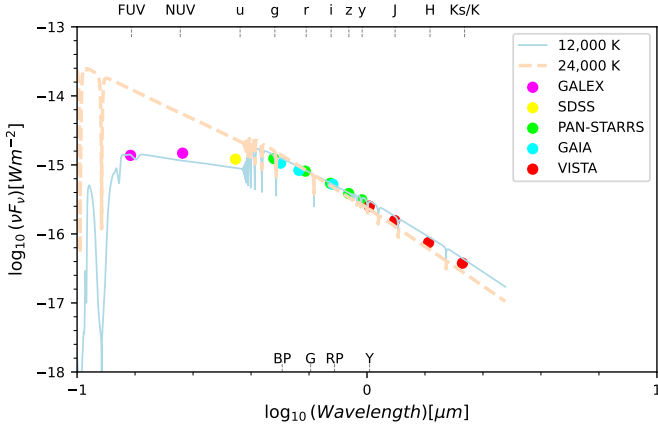


Fig. 11. SED fitting plot for WDJ100236.84+023835.03. The light blue curve represents the SED at about 12,000 K, while the light orange curve corresponds to about 24,000 K. In the FUV and NUV bands, the high-temperature curve is significantly higher than the observed data points.

spectra fitting. Manser et al. (2024) obtained its spectroscopic parameters with a temperature of approximately 10,008 K and $\log g$ of 8.65. When using *wdtools* for fitting with a temperature upper limit of 15,000 K, the results are 9992 K and 8.73 after 3D corrections, which are close to the ones provided by Manser et al. (2024). Figure 10 shows the fitting results from *wdtools* at both high and low temperatures. Clearly, based on the spectroscopic results, the fitting at higher temperature shows a better performance. However, based on the SED results, the fitting at the lower temperature shows a better performance. From SED fitting, we obtained a temperature for it of around 12,000 K, as is shown in Figure 11 and a radius of about $0.02R_{\odot}$.

Both spectral fitting and SED fitting match the corresponding WD template well, and the results from the double-DA model are approximately 13,000 K + 10,000 K, with the photometric radius of the primary star being about $0.015 R_{\odot}$, which is slightly better than the single-star fit. Thus, the possibility of a binary system is a plausible explanation, although direct observational evidence is currently lacking. Therefore, the cause of such a significant temperature discrepancy between the spectroscopic and photo-

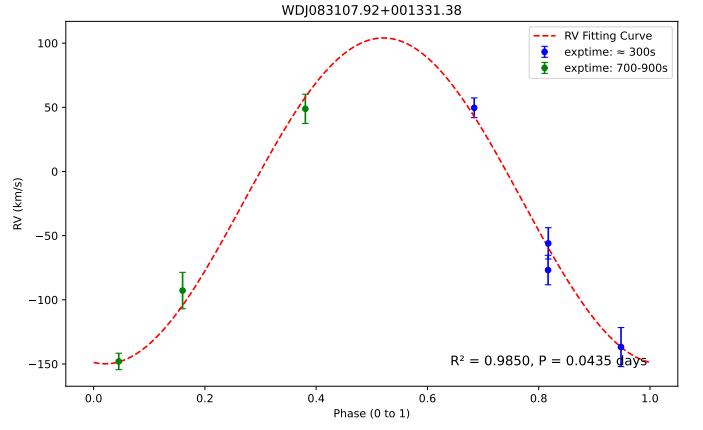


Fig. 12. RV fitting curve of WDJ083107.92+001331.38. The period is 0.0435 days, approximately 3750 s. The blue points correspond to an exposure time of about 300 s, accounting for less than 1/10 of the phase, while the green points correspond to an exposure time between 700 and 900 s, covering approximately 1/4 to 1/5 of the phase.

metric results still requires further investigation using additional high-resolution observational data.

6.2. ELM DWD candidates

WDJ083107.92+001331.38, the blue point at the top of the HR diagram Figure 1, was identified as a $0.2M_{\odot}$ -ELM through our multiple calculations. It exhibits significant RV variability, with a well-fit orbital period ranging from 0.0234 to 0.0532 days. Given the maximum exposure time of 900 s for its single-exposure spectra, and after examining the phase distribution and coverage, we concluded that the 0.0435-day period fit was more reliable, as is shown in Figure 12. However, considering that there are only seven data points, additional observations are necessary to determine a more accurate period.

Moreover, to search for additional potential ELMs, we cross-matched the DWD candidates with the ELM candidate catalog based on *Gaia* DR2 from Pelisoli & Vos (2019), and identified five common sources, which are marked as green points in Figure 13 and listed in Table 1. However, the current spectroscopic $\log g$ values of these green points are all greater than 7.0, which is beyond the typical ELM regime, as is shown in Table A.1. Therefore, considering their $\log g$ and the impact of the unseen companion, they remain potential ELM candidates rather than confirmed ELMs. Further spectroscopic observations are necessary to confirm their nature.

Table 1. BP-RP and GMAG of five crossmatched ELM candidates

WDJname	BP-RP	GMAG
WDJ092910.15+651429.78	-0.03762	10.8
WDJ093148.70+650304.99	-0.04296	10.7
WDJ093708.61+333404.69	-0.32278	8.8
WDJ125913.45+291653.60	0.07985	10.8
WDJ141625.94+311600.55	-0.07343	10.4
WDJ142332.30+511156.48	0.30816	11.8

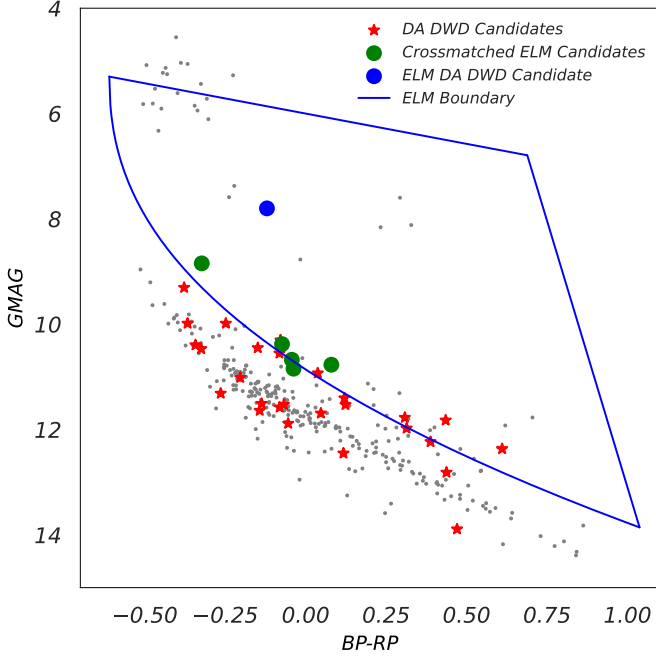


Fig. 13. Revised version of Figure 1. The blue line shows the initial boundary of ELM by Pelisoli & Vos (2019). The green points are the crossmatched ELM candidates. The blue point, WDJ083107.92+001331.38, is not present in Pelisoli & Vos (2019), likely because it was classified as a hot subdwarf in *Gaia* DR2 but as a WD in *Gaia* EDR3 (Geier et al. 2019; Gentile Fusillo et al. 2021).

6.3. Known DWDs (candidates)

We crossmatched our candidates with **Simbad** database and found five common sources in the literature. Among them, three have been confirmed as DWDs and two have been identified as DWD candidates.

WDJ093708.61+333404.69: This candidate was confirmed as a DWD by Brown et al. (2011), who obtained its $T_{\text{eff}} = 24,380\text{K}$ and mass = $0.38M_{\odot}$ from Liebert et al. (2005), provided 29 valid RV data points, calculated the RV variability from the F-test method, and obtained a period of 1.1142 days and a minimum companion mass of $0.5M_{\odot}$. From spectroscopic measurements, we derived $T_{\text{eff}} = 25,800\text{K}$ and $\log g = 7.55$, with a mass of $0.43M_{\odot}$. Its best-fit period calculated from Lomb-Scargle is 1.0740 days. Due to only seven exposures and the limited phase coverage of the RV, the reliability of the results is constrained. We combined these 29 data points with our seven measurements and recalculated the period using Lomb-Scargle, which yielded a period of 1.114162 days, with a sinusoidal fitting R^2 of only 0.85, as is shown in Fig 14.

WDJ094200.05+312920.27: This candidate was identified as a DWD candidate by Yan et al. (2024) based on significant RV variability, but no spectroscopic parameters and orbital parameters were provided. From spectral measurements, we obtained its $T_{\text{eff}} = 20,200\text{K}$, $\log g = 7.64$, and mass = $0.45M_{\odot}$. The first column of Figure 15 shows its fitting curves for five periods.

WDJ113100.20+493826.27: This candidate was identified as a single-lined DWD by Munday et al. (2024), who provided the parameters of the primary as $T_{\text{eff}} \approx 10,900\text{K}$ and $\log g \approx 7.7$, with $T_{\text{eff}} \approx 6900\text{K}$ of the companion. From spectral measurements, we obtained its $T_{\text{eff}} = 10,053\text{K}$, $\log g = 8.15$, and mass

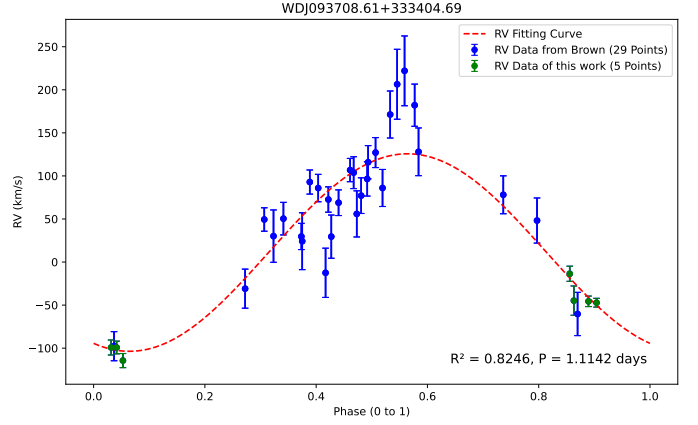


Fig. 14. RV fitting curve of WDJ093708.61+333404.69. The green points represent the RV data we calculated, while the blue points are from Brown et al. (2011). The period is 1.114167 days, consistent with the 1.1142-day period given by Brown et al. (2011), but the fit is suboptimal, with many outliers and an R^2 of only 0.82.

= $0.69M_{\odot}$. The second column of Figure 15 shows its fitting curves for five periods.

WDJ113941.32-004009.78: This candidate was identified as a DWD candidate by Yan et al. (2024) based on significant RV variability, but no spectroscopic parameters and orbital parameters were provided. From spectral measurements, we obtained its $T_{\text{eff}} = 26,414\text{K}$, $\log g = 7.5$, and mass = $0.42M_{\odot}$. The third column of Figure 15 shows its fitting curves for five periods.

WDJ141625.94+311600.55: This candidate was identified as a double-lined DWD by Munday et al. (2024), who calculated its $T_{\text{eff}} = 13,800\text{K}$, $\log g = 7.86$, and mass = $0.53M_{\odot}$ with a maximum period of 1.9 days and five exposures. From spectral measurements, we obtained its $T_{\text{eff}} = 14,602\text{K}$ and $\log g = 7.98$ with a mass of $0.60M_{\odot}$, also based on five exposures. Using the Lomb-Scargle method, we obtained the best-fit of 0.4127 days.

6.4. A potential triple-star system

The spectra of **WDJ121654.40-012920.77** exhibit features characteristic of an M-type star, as is shown in Figure 16. Pan-STARRS DR1 (Chambers et al. 2016) imaging also reveals a red star located about 2 arcseconds from the WD.

From *Gaia* DR3 (Gaia Collaboration 2022), we obtained the BP-RP, Gmag, plx, pm, pmRA, and pmDE for both stars, as is shown in Table 2. Additionally, from the *Gaia* HR diagram, it can be inferred that this star should be an early M-type star. Based on these data, we estimate the 3D distance between the two stars to be approximately 1-5 pc. Moreover, the system satisfies the kinematic criteria of the wide binary proposed by El-Badry & Rix (2018), but the photometric error slightly exceeds the standard threshold and is therefore not included in the catalog of El-Badry & Rix (2018). Nevertheless, we still suggest that the two stars are physically associated and may form a wide binary system.

However, at such a large 3D separation, it is implausible for the M-type star to induce the observed RV variation of $\Delta RV_{\text{max}} \approx 80\text{km/s}$. Instead, this variation is more likely caused by an unseen compact companion to the WD. Consequently, we propose that this system may be a wide triple-star system comprising a DWD and an early M-type star. Furthermore, contamination from this nearby early M-type star has compromised the

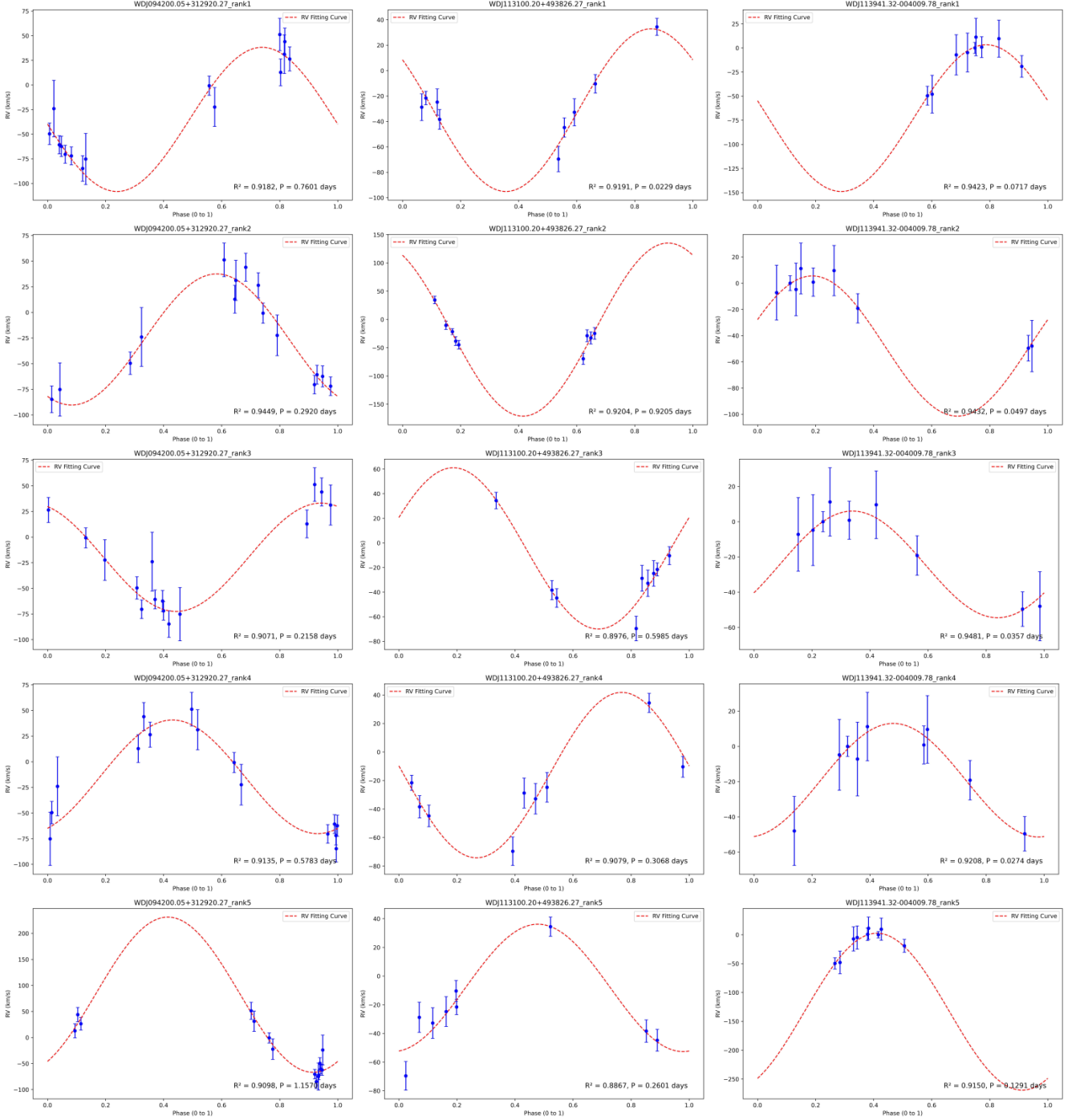


Fig. 15. RV fitting curves corresponding, from left to right, to WDJ094200.05+312920.27, WDJ113100.20+493826.27, and WDJ113941.32-004009.78. **WDJ094200.05+312920.27:** 15 valid exposures. The phase coverages of the rank-2 period (0.2920 days) and rank-4 period (0.5783 days) are better compared to the other three periods. **WDJ113100.20+493826.27:** Nine valid exposures, with the best-fit period being 0.0229 days (approximately 33 minutes). However, due to the limitations of the exposure time (500s–1400s), the reliability of this period is low. Other period plots have higher R^2 values but suffer from low phase coverage. **WDJ113941.32-004009.78:** Nine exposures. The phase coverages of the rank-3 period (0.0357 days) and the rank-4 period (0.0274 days) are relatively good, but their accuracy is affected by the exposure time. The phase coverages of the other three periods are low. Therefore, these three DWD candidates all require additional observations to determine more accurate periods.

photometric measurements of the WD, leaving insufficient reliable data in CDS for SED fitting.

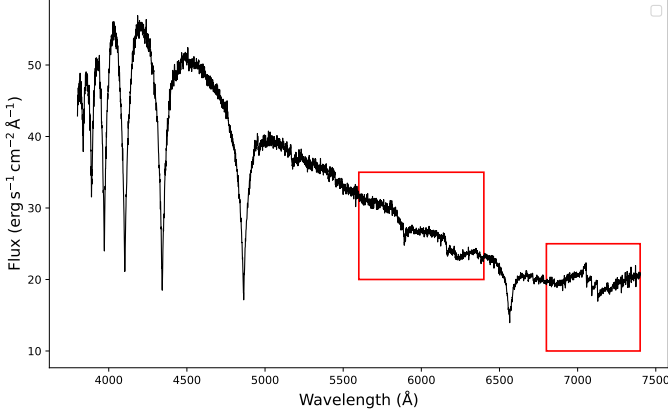
7. Conclusion

In this study, we have searched for DA DWD candidates by measuring spectroscopic RV and selecting sources with significant

RV variability. We crossmatched DESI EDR spectra with *Gaia* WD catalog to select DA samples with S/N greater than 10. Significant velocity variability were identified using the χ^2 variability metric, η . We fit the Balmer lines to measure the effective temperature and surface gravity, which were then interpolated to derive the masses, cooling ages, and radii. Orbital periods were

Table 2. Parameters of WDJ121654.40-012920.77 and the M-type Star.

	WD	M-type star
BP-RP	0.435026	2.435751
Gmag	17.9	15.9
plx (mas)	6.1391	6.3535
error_plx (mas)	0.1317	0.0427
pm (mas/yr)	41.299	41.698
pmRA (mas/yr)	-22.627	-22.43
error_pmRA (mas/yr)	0.173	0.058
pmDE (mas/yr)	-34.549	-35.152
error_pmDE (mas/yr)	0.103	0.036

**Fig. 16.** Coadded spectrum of WDJ121654.40-012920.77. In the wavelength range above 5000 Å, distinct features of an M-type star are observed, as is highlighted in the red boxes. This is likely caused by the contamination from the M-type star.

calculated using the Lomb-Scargle method, with five significant periods tentatively derived for each source. These periods were further fit with trigonometric functions to derive the corresponding semi-amplitudes. We further analyzed the photometric and SED properties to complement the spectroscopic analysis and enable a direct comparison with the derived spectroscopic parameters.

Finally, we identified 33 DAs exhibiting significant RV variability as DWD candidates, of which 28 were newly discovered, including 1 ELM DA and 1 source in a potential triple-star system. For 17 of the candidates, we derived well-constrained orbital periods and semi-amplitudes based on the current data. These findings further expand the known sample of DWD candidates.

We plan to conduct follow-up observations to further study our candidates and provide valuable observational data for future SNe Ia progenitor research. We also aim to use updated data, such as DESI DR1, along with more accurate binary star models, to identify additional unknown DWDs including non-DA double degenerates in the future.

Data availability

Tables in Appendix A represent only a small subset of the full data. More complete data are available on zenodo.org/records/15517675. Appendix B describes the online tables, which are only available in electronic form at the CDS via anonymous ftp to cdsarc.u-strasbg.fr (130.79.128.5) or via <http://cdsweb.u-strasbg.fr/cgi-bin/qcat?J/A+A/>.

Acknowledgements. This research is supported by the National Natural Science Foundation of China (12273056, 12090041, 11933004) and the National Key R&D Program of China (2022YFA1603002). Y.H.L. and B.Z.R. acknowledge support from the National Key R&D Program of China (Grant No. 2023YFA1607901).

This research used data obtained with the Dark Energy Spectroscopic Instrument (DESI). DESI construction and operations is managed by the Lawrence Berkeley National Laboratory. This material is based upon work supported by the U.S. Department of Energy, Office of Science, Office of High-Energy Physics, under Contract No. DE-AC02-05CH11231, and by the National Energy Research Scientific Computing Center, a DOE Office of Science User Facility under the same contract. Additional support for DESI was provided by the U.S. National Science Foundation (NSF), Division of Astronomical Sciences under Contract No. AST-0950945 to the NSF's National Optical-Infrared Astronomy Research Laboratory; the Science and Technology Facilities Council of the United Kingdom; the Gordon and Betty Moore Foundation; the Heising-Simons Foundation; the French Alternative Energies and Atomic Energy Commission (CEA); the National Council of Science and Technology of Mexico (CONACYT); the Ministry of Science and Innovation of Spain (MICINN), and by the DESI Member Institutions: www.desi.lbl.gov/collaborating-institutions. The DESI collaboration is honored to be permitted to conduct scientific research on Iolkam Du'ag (Kitt Peak), a mountain with particular significance to the Tohono O'odham Nation. Any opinions, findings, and conclusions or recommendations expressed in this material are those of the author(s) and do not necessarily reflect the views of the U.S. National Science Foundation, the U.S. Department of Energy, or any of the listed funding agencies. This work has made use of data from the European Space Agency (ESA) mission *Gaia* (<https://www.cosmos.esa.int/gaia>), processed by the *Gaia* Data Processing and Analysis Consortium (DPAC, <https://www.cosmos.esa.int/web/gaia/dpac/consortium>). Funding for the DPAC has been provided by national institutions, in particular the institutions participating in the *Gaia* Multilateral Agreement.

We acknowledge use of the VizieR catalog access tool, operated at CDS, Strasbourg, France, and of Astropy, a community-developed core Python package for Astronomy (Astropy Collaboration, 2013). We also acknowledge data from the Zwicky Transient Facility (ZTF, <https://www.ztf.caltech.edu>), funded equally by the U.S. National Science Foundation and an international consortium of universities and institutions.

References

- Adame, A. G., Aguilar, J., Ahlen, S., et al. 2024, *AJ*, 168, 58
- Ahumada, R., Allende Prieto, C., Almeida, A., et al. 2020, *ApJS*, 249, 3
- Althaus, L. G., Córscico, A. H., Isern, J., & García-Berro, E. 2010, *A&A Rev.*, 18, 471
- Althaus, L. G., Miller Bertolami, M. M., & Córscico, A. H. 2013, *A&A*, 557, A19
- Anguiano, B., Rebassa-Mansergas, A., García-Berro, E., et al. 2017, *MNRAS*, 469, 2102
- Arseneau, S., Chandra, V., Hwang, H.-C., et al. 2024, *ApJ*, 963, 17
- Badenes, C. & Maoz, D. 2012, *ApJ*, 749, L11
- Bellm, E. C., Kulkarni, S. R., Graham, M. J., et al. 2019, *PASP*, 131, 018002
- Bergeron, P., Saffer, R. A., & Liebert, J. 1992, *ApJ*, 394, 228
- Bianchi, L., Shiao, B., & Thilker, D. 2017, *ApJS*, 230, 24
- Blouin, S., Dufour, P., & Kowalski, P. M. 2017, in *Astronomical Society of the Pacific Conference Series*, Vol. 509, 20th European White Dwarf Workshop, ed. P. E. Tremblay, B. Gaensicke, & T. Marsh, 227
- Bours, M. C. P., Marsh, T. R., Parsons, S. G., et al. 2014, *MNRAS*, 438, 3399
- Bragaglia, A., Greggio, L., Renzini, A., & D'Odorico, S. 1990, *ApJ*, 365, L13
- Breedt, E., Steeghs, D., Marsh, T. R., et al. 2017, *MNRAS*, 468, 2910
- Breivik, K., Kremer, K., Bueno, M., et al. 2018, *ApJ*, 854, L1
- Brown, J. M., Kilic, M., Brown, W. R., & Kenyon, S. J. 2011, *ApJ*, 730, 67
- Brown, W. R., Kilic, M., Allende Prieto, C., & Kenyon, S. J. 2010, *ApJ*, 723, 1072
- Brown, W. R., Kilic, M., Kosakowski, A., et al. 2020, *ApJ*, 889, 49
- Brown, W. R., Kilic, M., Kosakowski, A., & Gianninas, A. 2022, *ApJ*, 933, 94
- Burdge, K. B., Coughlin, M. W., Fuller, J., et al. 2020, *ApJ*, 905, L7
- Burdge, K. B., Coughlin, M. W., Fuller, J., et al. 2019, *Nature*, 571, 528–531
- Burdge, K. B., Prince, T. A., Fuller, J., et al. 2020, *ApJ*, 905, 32
- Bédard, A., Bergeron, P., Brassard, P., & Fontaine, G. 2020, *ApJ*, 901, 93
- Caldwell, R. R. 2002, *Physics Letters B*, 545, 23
- Camisassa, M. E., Althaus, L. G., Córscico, A. H., et al. 2019, *A&A*, 625, A87
- Chambers, K. C., Magnier, E. A., Metcalfe, N., et al. 2016, *arXiv e-prints*, arXiv:1612.05560
- Chandra, V. 2020, *wdtools: Computational Tools for the Spectroscopic Analysis of White Dwarfs*
- Chandra, V., Hwang, H.-C., Zakamska, N. L., & Budavári, T. 2020, *MNRAS*, 497, 2688

- Cheng, S. 2021, *WD_models*: A Python package for transformations between WD photometry and physical parameters
- Cutri, R. M., Skrutskie, M. F., van Dyk, S., et al. 2003, *2MASS All Sky Catalog of point sources*.
- Dey, A., Schlegel, D. J., Lang, D., et al. 2019, *AJ*, 157, 168
- Drake, A. J., Djorgovski, S. G., Mahabal, A., et al. 2009, *ApJ*, 696, 870
- Dufour, P., Blouin, S., Coutu, S., et al. 2017, in *Astronomical Society of the Pacific Conference Series*, Vol. 509, 20th European White Dwarf Workshop, ed. P. E. Tremblay, B. Gänsicke, & T. Marsh, 3
- Eggleton, P. P. 1983, *ApJ*, 268, 368
- El-Badry, K. & Rix, H.-W. 2018, *MNRAS*, 480, 4884
- El-Badry, K., Rix, H.-W., & Heintz, T. M. 2021, *MNRAS*, 506, 2269
- Foley, R. J., Challis, P. J., Chornock, R., et al. 2013, *ApJ*, 767, 57
- Foss, D. 1989, in *IAU Colloq. 114: White Dwarfs*, ed. G. Wegner, Vol. 328, 163
- Gaia Collaboration. 2022, *VizieR Online Data Catalog: Gaia DR3 Part 1. Main source* (Gaia Collaboration, 2022), *VizieR On-line Data Catalog: I/355*. Originally published in: doi:10.1051/0004-63
- Gaia Collaboration, Prusti, T., de Bruijn, J. H. J., et al. 2016, *A&A*, 595, A1
- Gaia Collaboration, Vallenari, A., Brown, A. G. A., et al. 2023, *A&A*, 674, A1
- Geier, S., Raddi, R., Gentile Fusillo, N. P., & Marsh, T. R. 2019, *A&A*, 621, A38
- Gentile Fusillo, N. P., Tremblay, P.-E., Gänsicke, B. T., et al. 2019, *MNRAS*, 482, 4570
- Gentile Fusillo, N. P., Tremblay, P.-E., Cukanovaite, E., et al. 2021, *MNRAS*, 508, 3877–3896
- Georgousi, M., Karnesis, N., Korol, V., Pieroni, M., & Stergioulas, N. 2023, *MNRAS*, 519, 2552
- Gomel, R., Faigler, S., & Mazeh, T. 2021, *MNRAS*, 501, 2822
- Graham, M. J., Kulkarni, S. R., Bellm, E. C., et al. 2019, *PASP*, 131, 078001
- Green, G. 2018, *The Journal of Open Source Software*, 3, 695
- Green, G. M., Schlafly, E., Zucker, C., Speagle, J. S., & Finkbeiner, D. 2019, *ApJ*, 887, 93
- Han, Z. & Podsiadlowski, P. 2004, *MNRAS*, 350, 1301
- Han, Z., Podsiadlowski, P., & Eggleton, P. P. 1995, *MNRAS*, 272, 800
- Hillebrandt, W., Kromer, M., Röpke, F. K., & Ruiter, A. J. 2013, *Frontiers of Physics*, 8, 116
- Holberg, J. B. & Bergeron, P. 2006, *AJ*, 132, 1221
- Hoyle, F. & Fowler, W. A. 1960, *ApJ*, 132, 565
- Iben, Jr., I. & Tutukov, A. V. 1984, *ApJ*, 284, 719
- Jin, H.-M., Ma, B., Shao, Y., & Wang, Y. 2025, *MNRAS*, 536, 2770
- Kashi, A. & Soker, N. 2011, *MNRAS*, 417, 1466
- Keller, P. M., Breedt, E., Hodgkin, S., et al. 2022, *MNRAS*, 509, 4171
- Kepler, S. O., Pelisoli, I., Koester, D., et al. 2015, *MNRAS*, 455, 3413
- Kleinman, S. J., Harris, H. C., Eisenstein, D. J., et al. 2004, *ApJ*, 607, 426
- Kleinman, S. J., Kepler, S. O., Koester, D., et al. 2013, *ApJS*, 204, 5
- Kochanek, C. S., Shappee, B. J., Stanek, K. Z., et al. 2017, *PASP*, 129, 104502
- Koester, D. 2010, *Mem. Soc. Astron. Italiana*, 81, 921
- Koester, D., Napiwotzki, R., Christlieb, N., et al. 2001, *A&A*, 378, 556
- Koester, D., Voss, B., Napiwotzki, R., et al. 2009, *A&A*, 505, 441
- Korol, V., Belokurov, V., & Toonen, S. 2022, *MNRAS*, 515, 1228–1246
- Korol, V., Rossi, E. M., Groot, P. J., et al. 2017, *MNRAS*, 470, 1894
- Kosakowski, A., Brown, W. R., Kilic, M., et al. 2023, *ApJ*, 950, 141
- Kosakowski, A., Kilic, M., Brown, W. R., & Gianninas, A. 2020, *ApJ*, 894, 53
- Kowalski, P. M. & Saumon, D. 2006, *ApJ*, 651, L137–L140
- Lawrence, A., Warren, S. J., Almaini, O., et al. 2007, *MNRAS*, 379, 1599
- Li, Z., Chen, X., Chen, H.-L., & Han, Z. 2019, *ApJ*, 871, 148
- Li, Z., Chen, X., Chen, H.-L., et al. 2020, *ApJ*, 893, 2
- Li, Z., Chen, X., Ge, H., Chen, H.-L., & Han, Z. 2023, *A&A*, 669, A82
- Liebert, J., Bergeron, P., & Holberg, J. B. 2005, *ApJS*, 156, 47
- Liebert, J. & Sion, E. M. 1994, in *Astronomical Society of the Pacific Conference Series*, Vol. 60, *The MK Process at 50 Years: A Powerful Tool for Astrophysical Insight*, ed. C. J. Corbally, R. O. Gray, & R. F. Garrison, 64
- Liu, D., Wang, B., & Han, Z. 2018, *MNRAS*, 473, 5352
- Liu, Z.-W., Röpke, F. K., & Han, Z. 2023, *RAA*, 23, 082001
- Livio, M. & Soker, N. 1988, *ApJ*, 329, 764
- Lomb, N. R. 1976, *Ap&SS*, 39, 447
- Maeda, K. & Terada, Y. 2016, *International Journal of Modern Physics*, 25, 1630024
- Manser, C. J., Izquierdo, P., Gänsicke, B. T., et al. 2024, *MNRAS*, 535, 254
- Maoz, D. & Hallakoun, N. 2017, *MNRAS*, 467, 1414
- Maoz, D. & Mannucci, F. 2012, *PASA*, 29, 447
- Maoz, D., Mannucci, F., & Nelemans, G. 2014, *ARA&A*, 52, 107
- Marsh, T. R. 1995, *MNRAS*, 275, L1
- Maschi, F. J., Laher, R. R., Rusholme, B., et al. 2019, *PASP*, 131, 018003
- Maxted, P. F. L. & Marsh, T. R. 1999, *MNRAS*, 307, 122
- Maxted, P. F. L., Marsh, T. R., & Moran, C. K. J. 2000, *MNRAS*, 319, 305
- McCook, G. P. & Sion, E. M. 1999, *ApJS*, 121, 1
- McCracken, H. J., Milvang-Jensen, B., Dunlop, J., et al. 2012, *A&A*, 544, A156
- Munday, J., Pelisoli, I., Tremblay, P. E., et al. 2024, *MNRAS*, 532, 2534
- Munday, J., Tremblay, P. E., Hermes, J. J., et al. 2023, *MNRAS*, 525, 1814
- Napiwotzki, R., Christlieb, N., Drechsel, H., et al. 2001, *Astronomische Nachrichten*, 322, 411
- Napiwotzki, R., Karl, C. A., Lisker, T., et al. 2020, *A&A*, 638, A131
- Nelemans, G., Napiwotzki, R., Karl, C., et al. 2005, *A&A*, 440, 1087
- Nomoto, K., Thielemann, F. K., & Yokoi, K. 1984, *ApJ*, 286, 644
- O’Brien, M. W., Tremblay, P. E., Klein, B. L., et al. 2024, *MNRAS*, 527, 8687
- Ofek, E. O., Soumagnac, M., Nir, G., et al. 2020, *MNRAS*, 499, 5782
- Pelisoli, I. & Vos, J. 2019, *MNRAS*, 488, 2892
- Perlmutter, S., Aldering, G., Goldhaber, G., et al. 1999, *ApJ*, 517, 565
- Planck Collaboration, Ade, P. A. R., Aghanim, N., et al. 2016, *A&A*, 594, A13
- Pylyser, E. & Savonije, G. J. 1988, *A&A*, 191, 57
- Raddi, R., Hollands, M. A., Koester, D., et al. 2019, *MNRAS*, 489, 1489
- Raddi, R., Rebassa-Mansergas, A., Torres, S., et al. 2025, *A&A*, 695, A131
- Rebassa-Mansergas, A., Toonen, S., Korol, V., & Torres, S. 2019, *MNRAS*, 482, 3656
- Ren, L., Li, C., Ma, B., et al. 2023, *ApJS*, 264, 39
- Ricker, G. R., Winn, J. N., Vanderspek, R., et al. 2015, *Journal of Astronomical Telescopes, Instruments, and Systems*, 1, 014003
- Riess, A. G., Filippenko, A. V., Challis, P., et al. 1998, *AJ*, 116, 1009
- Riess, A. G., Strolger, L.-G., Tonry, J., et al. 2004, *ApJ*, 607, 665
- Saffer, R. A., Liebert, J., & Olszewski, E. W. 1988, *ApJ*, 334, 947
- Scargle, J. D. 1982, *ApJ*, 263, 835
- Shen, K. J., Boubert, D., Gänsicke, B. T., et al. 2018, *ApJ*, 865, 15
- Soker, N. 2019, *New A Rev.*, 87, 101535
- Sousa, M. F., Goulart Coelho, J., de Araújo, J. C., Guidorzi, C., & Rueda, J. A. 2024, in *What Was That? - Planning ESO Follow up for Transients, Variables, and Solar System Objects in the Era of LSST*, 2
- Steinfadt, J. D. R., Kaplan, D. L., Shporer, A., Bildsten, L., & Howell, S. B. 2010, *ApJ*, 716, L146
- Tonry, J. L. & Davis, M. 1979, *AJ*, 84, 1511
- Torres, S., Canals, P., Jiménez-Esteban, F. M., Rebassa-Mansergas, A., & Solano, E. 2022, *MNRAS*, 511, 5462
- Torres, S., Cruz, P., Murillo-Ojeda, R., et al. 2023, *A&A*, 677, A159
- Tremblay, P.-E., Bergeron, P., & Gianninas, A. 2011, *ApJ*, 730, 128
- Tremblay, P. E., Ludwig, H. G., Steffen, M., & Freytag, B. 2013, *A&A*, 559, A104
- Vennes, S., Nemeth, P., Kawka, A., et al. 2017, *Science*, 357, 680
- Wang, B. & Han, Z. 2012, *New A Rev.*, 56, 122
- Wang, B., Justham, S., & Han, Z. 2013, *A&A*, 559, A94
- Wang, T., Liu, G., Cai, Z., et al. 2023, *Science China Physics, Mechanics, and Astronomy*, 66, 109512
- Webbink, R. F. 1984, *ApJ*, 277, 355
- Werner, K., El-Badry, K., Gänsicke, B. T., & Shen, K. J. 2024, *A&A*, 689, L6
- Whelan, J. & Iben, Jr., I. 1973, *ApJ*, 186, 1007
- Yan, H., Zhao, J., Shi, W., et al. 2024, *A&A*, 684, A103
- Yuan, H., Li, Z., Bai, Z., et al. 2023a, *MNRAS*, 526, 5471
- Yuan, H., Li, Z., Bai, Z., et al. 2023b, *AJ*, 165, 119
- Yungelson, L. R., Livio, M., Tutukov, A. V., & Saffer, R. A. 1994, *ApJ*, 420, 336
- Zucker, S. 2003, *MNRAS*, 342, 1291–1298

Appendix A: Additional material

Table A.1. Basic parameters of 33 DA DWD candidates with significant RV variability.

WDJname	ra	dec	η ¹	n_{exp}	$\Delta RV_{max}(km/s)$	$T_{eff}(K)$	$\log g$	mass(M_{\odot})	$age_{cool}(Gyr)$
WDJ072212.06+412549.15	110.550113	41.430252	9.36	9	98	14102±647	8.43±0.13	0.88±0.08	0.513±0.139
WDJ083039.46+324147.23	127.663377	32.693352	2.89	12	44	6969±214	8.14±0.27	0.69±0.16	2.350±1.053
WDJ083107.92+001331.38	127.782978	0.225361	inf	7	198	16198±748	6.52±0.28	0.20±0.07	— ²
WDJ084031.47+214042.73	130.130897	21.678454	4.81	10	122	17071±713	8.54±0.08	0.95±0.05	0.354±0.064
WDJ084253.03+230025.47	130.720837	23.006570	8.26	10	50	26656±818	7.96±0.16	0.62±0.08	0.016±0.007
WDJ092910.15+651429.78	142.291777	65.241481	3.02	13	48	15274±766	7.84±0.11	0.53±0.06	0.148±0.041
WDJ093000.81+651412.56	142.503169	65.236727	5.93	16	98	24940±1438	8.14±0.21	0.72±0.12	0.042±0.030
WDJ093148.70+650304.99	142.952666	65.051292	6.81	12	60	16796±497	7.91±0.21	0.58±0.11	0.126±0.056
WDJ093649.57+655031.43	144.206331	65.841944	3.15	26	116	16864±781	8.30±0.17	0.81±0.11	0.255±0.088
WDJ093708.61+333404.69	144.285554	33.567769	inf	7	101	25737±892	7.55±0.07	0.43±0.03	0.011±0.002
WDJ094200.05+312920.27	145.500221	31.488876	inf	15	136	20225±477	7.64±0.11	0.45±0.05	0.032±0.007
WDJ100236.84+023835.03	150.653515	2.642941	8.99	17	143	23878±1071	8.30±0.17	0.81±0.11	0.076±0.040
WDJ100438.88+022022.87	151.161887	2.339897	11.84	11	112	6767±162	7.72±0.44	0.49±0.19	1.566±0.997
WDJ105824.35+512738.87	164.601249	51.460624	7.41	14	61	13569±1282	8.18±0.10	0.72±0.06	0.382±0.117
WDJ113100.20+493826.27	172.750593	49.640633	inf	9	104	10053±651	8.15±0.15	0.69±0.10	0.815±0.268
WDJ113941.32+004009.78	174.922261	-0.669505	3.17	9	61	26414±1215	7.50±0.10	0.42±0.04	0.009±0.003
WDJ120347.43+002310.94	180.946997	-0.386537	inf	25	91	21250±621	8.47±0.14	0.92±0.08	0.169±0.052
WDJ121654.40+012920.77	184.226538	-1.489306	3.14	20	78	17538±1373	7.71±0.33	0.50±0.15	0.086±0.063
WDJ122337.56+333806.54	185.906341	33.634979	2.68	13	51	10095±174	8.30±0.16	0.79±0.10	1.046±0.331
WDJ123515.68+550317.93	188.815850	55.054837	3.87	9	70	8829±64	8.08±0.15	0.65±0.09	1.016±0.235
WDJ125913.45+291653.60	194.805830	29.281324	10.65	10	147	10167±121	7.97±0.29	0.60±0.16	0.656±0.309
WDJ141625.94+311600.55	214.107822	31.266742	3.33	5	43	14602±352	7.98±0.07	0.60±0.04	0.216±0.030
WDJ141807.16+514354.43	214.529882	51.731748	inf	11	145	20006±827	7.96±0.11	0.60±0.06	0.063±0.021
WDJ142006.30+532234.22	215.026846	53.375724	6.87	6	52	7231±25	8.06±0.04	0.63±0.02	1.586±0.097
WDJ142332.30+511156.48	215.883157	51.198562	12.38	13	68	8589±144	7.85±0.27	0.52±0.14	0.835±0.334
WDJ144038.41+154054.32	220.159987	15.681602	2.61	5	41	18100±575	8.14±0.05	0.70±0.03	0.141±0.021
WDJ145655.24+525805.49	224.229890	52.968350	9.12	5	65	17300±258	7.78±0.05	0.50±0.02	0.077±0.009
WDJ154710.84+442848.23	236.795079	44.480054	inf	10	125	10023±156	8.32±0.13	0.81±0.09	1.098±0.313
WDJ155852.79+421052.05	239.719989	42.180941	5.65	9	69	13726±1013	8.31±0.16	0.81±0.09	0.467±0.147
WDJ161737.30+534859.08	244.405114	53.816475	inf	11	122	7762±92	7.68±0.34	0.46±0.16	0.957±0.497
WDJ162825.98+333450.65	247.108050	33.580674	3.96	10	83	25523±874	8.03±0.16	0.65±0.08	0.023±0.011
WDJ172428.42+583538.97	261.117660	58.594140	4.54	14	52	11576±1003	8.06±0.19	0.65±0.11	0.513±0.192
WDJ175912.93+611257.59	269.803801	61.215980	13.33	8	134	17460±524	7.93±0.16	0.58±0.08	0.108±0.037

¹ The "inf" in the η column indicates that P in Equation 3.4 is very small, close to 0. When performing logarithmic calculations in Python, η approaches infinity and is therefore marked as "inf" in our results.

² Missing parameters are due to the interpolation sequence not providing the cooling age of ELM. The parameters of this ELM were calculated using the He-core model from Althaus et al. (2013). If we use the CO-core model from Bédard et al. (2020) for the calculation, the result obtained will be $mass = 0.27 \pm 0.03 M_{\odot}$ and $age_{cool} = 0.013 \pm 0.013 Gyr$. It is still an ELM.

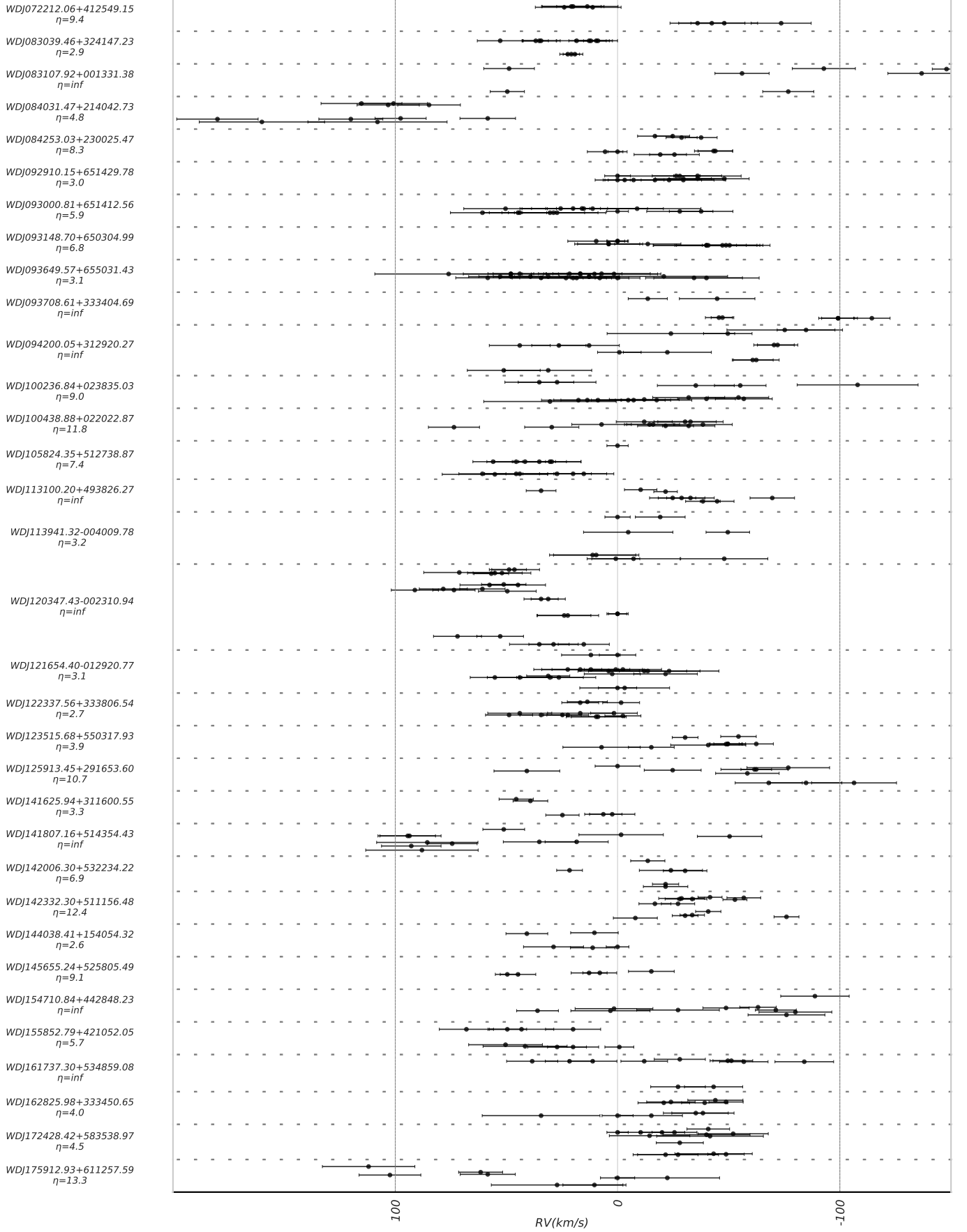


Fig. A.1. RVs measured for the 33 DA DWD candidates with significant RV variability. The object names and the corresponding η values are provided in the left. The "inf" means a very large η .

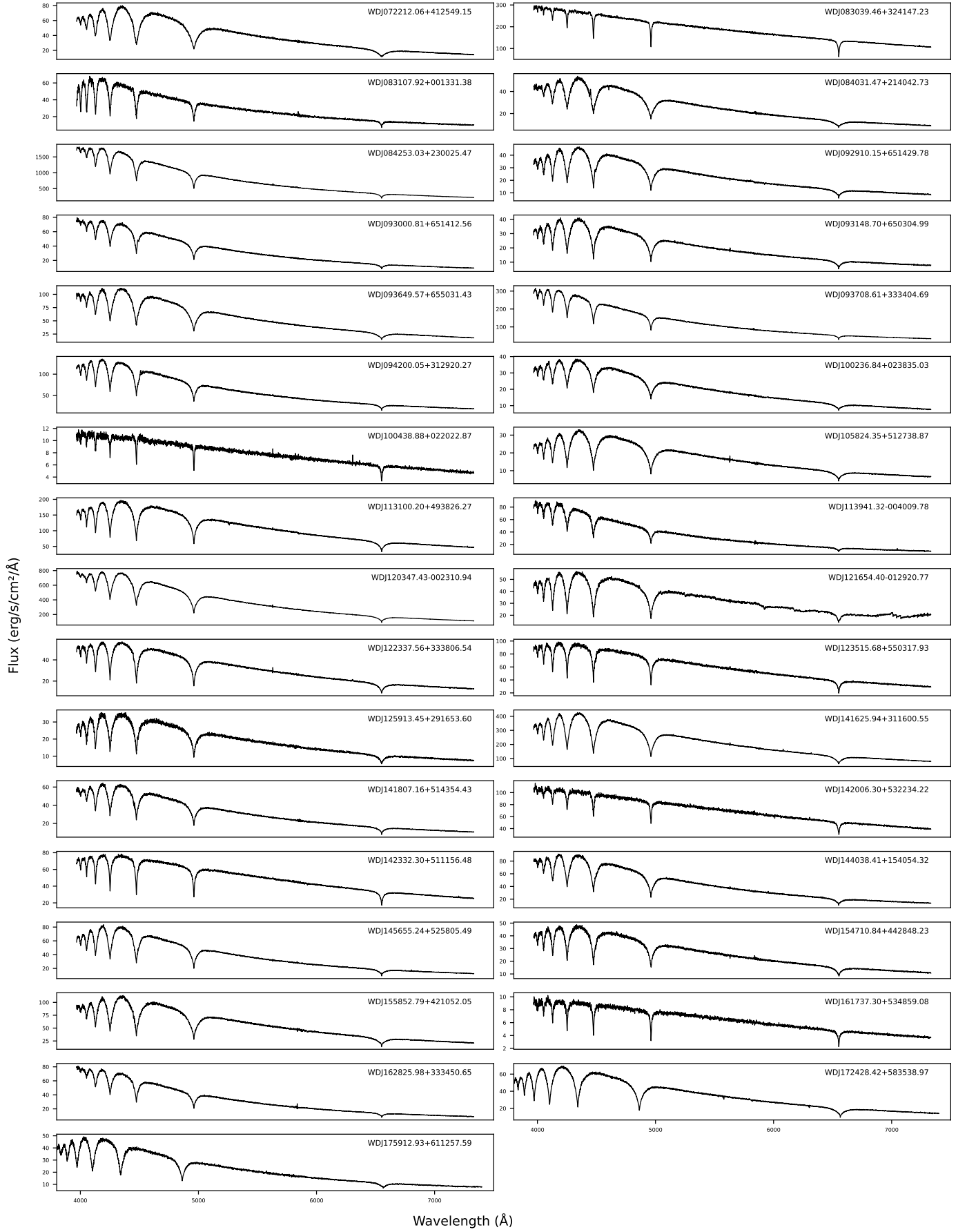


Fig. A.2. Coadded spectra of the 33 DA DWD candidates with wavelength from 3800 Å to 7500 Å.

Table A.2. Periods and semi-amplitudes of 17 DWD candidates with well-fit periodic curves. The unit of the period is day, and the semi-amplitude is measured in km/s.

WDJname	p1	k1	p2	k2	p3	k3	p4	k4	p5	k5
WDJ083107.92+001331.38	0.025833	101.7	0.023362	102.9	0.053154	166.7	0.105125	401.9	0.04345	126.9
WDJ084031.47+214042.73	0.117605	67.4	0.133335	73.6	0.105195	62.1	0.153924	80.9	0.095155	58.0
WDJ084253.03+230025.47	0.392901	24.5	0.281881	23.7	0.648206	25.5	0.219779	23.0	1.851094	26.5
WDJ094200.05+312920.27	0.760139	73.2	0.291952	63.9	0.215751	52.8	0.578282	55.4	1.156983	149.0
WDJ100236.84+023835.03	9.985434	48.2	9.95	47.4	10.05001	49.7	9.85	45.5	10.15001	52.3
WDJ100438.88+022022.87	0.432368	54.8	0.759571	53.8	0.755	52.0	0.765	56.1	0.435	58.0
WDJ113100.20+493826.27	0.022874	64.0	0.920477	153.2	0.598473	65.5	0.306755	58.0	0.26012	44.4
WDJ113941.32-004009.78	0.071727	76.0	0.049662	53.5	0.035688	30.3	0.027432	32.2	0.129075	136.0
WDJ122337.56+333806.54	0.057603	21.6	0.054458	21.9	0.065124	20.6	0.075286	19.6	0.088667	19.2
WDJ123515.68+550317.93	0.094437	25.0	0.081942	26.3	0.1741	30.2	0.157703	25.1	1.137271	29.0
WDJ125913.45+291653.60	0.353925	74.7	0.546427	58.5	0.897612	70.8	0.177292	59.7	0.110555	60.4
WDJ141625.94+311600.55	0.412656	46.1	0.179616	26.1	0.048265	27.4	0.03689	67.8	0.219018	29.3
WDJ141807.16+514354.43	0.545691	69.6	0.250345	79.2	0.687871	87.1	0.333801	99.0	0.500696	181.3
WDJ142006.30+532234.22	0.177773	32.4	0.026334	26.3	0.056697	28.0	0.100007	66.0	0.068664	31.1
WDJ154710.84+442848.23	0.038801	67.7	0.130647	48.9	0.150352	49.0	0.115499	50.8	0.177072	50.5
WDJ162825.98+333450.65	0.157652	100.7	0.07883	33.4	0.085611	33.2	0.187342	91.3	0.073051	31.4
WDJ175912.93+611257.59	0.59808	75.5	0.374359	81.0	0.061575	61.8	1.487426	71.5	0.065616	57.2

Appendix B: Description of the online tables

Table B.1: Catalog extension one: RVs of single-exposure spectra.

Column	Heading	Description
1	WDJname	WDJ + J2000 ra (hh mm ss.ss) + dec (dd mm ss.ss), equinox and epoch 2000
2	mjd	MJD identifier for a unique DESI spectrum
3	median_snr	Median S/N for a unique DESI spectrum
4	velocity	RV (km/s) obtained from CCF of template-matching
5	velocity_error	Error (km/s) of RV obtained from Equation 2

Table B.2: Catalog extension two: extended section of Table A.1.

Column	Heading	Description
1	WDJname	WDJ + J2000 ra (hh mm ss.ss) + dec (dd mm ss.ss), equinox and epoch 2000
2	ra	Right Ascension J2000 (degrees)
3	dec	Declination J2000 (degrees)
4	Gmag	<i>Gaia</i> EDR3 G-band mean magnitude
5	plx	<i>Gaia</i> EDR3 Absolute stellar parallax (mas) at Ep=2016.0
6	BP-RP	<i>Gaia</i> EDR3 BP-RP colour
7	GMAG	<i>Gaia</i> EDR3 Absolute G magnitude
8	E(B-V)	3D extinction obtained from <i>dustmaps</i> (Green 2018)
9	n	Number of observations
10	eta	RV Variability parameter η in Equation 3.4
11	deltarv	Maximum difference in RV
12	Teff1d	Effective temperature (K) obtained from <i>wdtools</i> (Chandra et al. 2020; Chandra 2020)
13	Teff1d_er	Error of effective temperature (K) obtained from <i>wdtools</i>
14	logg1d	Surface gravity obtained from <i>wdtools</i>
15	logg1d_er	Error of surface gravity obtained from <i>wdtools</i>
16	Teff	Effective temperature (K) after 3D corrections (Tremblay et al. 2013)
17	logg	Surface gravity after 3D corrections (Tremblay et al. 2013)
18	Teff_er	Error (K) of Column 16
19	logg_er	Error of Column 17
20	mass	Mass (M_{\odot}) obtained by interpolating Column 16 and Column 17 into WD evolutionary models
21	mass_er	Error (M_{\odot}) of Column 20
22	age_cool	Cooling age (Gyr) obtained by interpolating Column 16 and Column 17 into WD evolutionary models
23	age_cool_er	Error (Gyr) of Column 22
24	r_sp	Radius (R_{\odot}) obtained by interpolating Column 16 and Column 17 into WD evolutionary models
25	r_sp_er	Error (R_{\odot}) of Column 24
26	Teff_sed	Effective temperature (K) obtained from the single-DA SED fitting
27	r_sed	Radius (R_{\odot}) obtained from the single-DA SED fitting
28	Teff_desi_sp_1d	Effective temperature (K) from DESI spectroscopic fitting by Manser et al. (2024)
29	logg_desi_sp_1d	Surface gravity from DESI spectroscopic fitting by Manser et al. (2024)
30	Teff_desi_sp_3d	Effective temperature (K) after 3D corrections from DESI spectroscopic fitting by Manser et al. (2024)
31	logg_desi_sp_3d	Surface gravity after 3D corrections from DESI spectroscopic fitting by Manser et al. (2024)
32	r_desi	Radius (R_{\odot}) obtained by interpolating Column 30 and Column 31 into WD evolutionary models

Table B.3: Catalog extension three: orbital parameters for 33 DWD candidates.

Column	Heading	Description
1	WDJname	WDJ + J2000 ra (hh mm ss.ss) + dec (dd mm ss.ss), equinox and epoch 2000
2	period	Period (days) obtained from the Lomb-Scargle method
3	rank	Power spectrum rank of the period
4	K	Semi-amplitude (km/s) corresponding to the period
5	R2	R^2 of the fitting curve.